Palacký University Olomouc
Faculty of Science

Department of Optics

Optical superresolution by image synthesis

Master's Thesis

Filip Juráň

Palacký University Olomouc
Faculty of Science

Department of Optics

Optical superresolution by image synthesis

Master's Thesis

Author:	Bc. Filip Juráň
Study programme:	B1701 Physics
Field of study:	Optics and Optoelectronics
Form of study:	Full-time
Supervisor:	RNDr. Miroslav Ježek, Ph.D.
Cosupervisor:	Mgr. Jaromír Běhal, Ph.D.

Thesis submitted on: . . . .

Univerzita Palackého
Přírodovědecká fakulta

Katedra optiky

Zlepšení optického rozlišení syntézou obrazu

Diplomová práce

Autor:	Bc. Filip Juráň
Studijní program:	B1701 Fyzika
Studijní obor:	Optika a optoelektronika
Forma studia:	Prezenční
Vedoucí:	RNDr. Miroslav Ježek, Ph.D.
Konzultant:	Mgr. Jaromír Běhal, Ph.D.

Práce odevzdána dne: ....

Abstract

Optical super-resolution by image synthesis based on maximum likelihood estimation is presented. A fundamental imaging optical system, a lens with a finite aperture, is studied. The intensity images are acquired at various distances and transversal shifts. The object mutual intensity is reconstructed from all intensity scans. Numerical simulations are carried out to show the experimental feasibility. They also touch on the efficiency of the problematics. Furthermore, an experiment is performed. Structures with separation 6x under the Rayleigh limit are resolved.

Keywords

Acknowledgments

I am very thankful to be working under my supervisor, Miroslav Ježek. I thank him for his great guidance and advice in and outside my studies. I would also love to thank my cosuperviser Jaromír Běhal, for his friendly attitude, for helping me with the experiment, and for teaching me useful tips and tricks in the optical laboratory. Special thanks goes to my parents and the whole family for their inextinguishable support and for keeping my spirits high.

FILIP JURÁŇ

Declaration

I hereby declare that I have written this Master's Thesis and performed all the presented research and experimental tasks by myself, while being supervised by RNDr. Miroslav Ježek, Ph.D. I also state that every resource used is properly cited. I agree with the Thesis being used for teaching purposes and being made available at the website of the Department of Optics.

Signed in Olomouc on . . . .

FILIP JURÁŇ

Contents

Chapter 1

Introduction

Any real imaging system is subjected to diffraction, owing to its finite aperture. Diffraction then limits the spatial resolution as points in the object are imaged as spots, resulting in image blurring. This blurring can be quantified, among others, by the Abbe criterion (supposing coherent light) or the Rayleigh criterion (supposing incoherent light). The latter states that two point-like sources are considered resolved when a maximum of the first source falls into the minimum of the second source. There are then multiple ways how to approach super-resolution, depending on how we define the problem. If the goal is to determine the distance between two (unresolved) point sources, we would talk about parameter estimation. Another possible task is when two or more (unresolved) objects are known and one is trying to construct an optimal measurement that would determine which object is present, we would talk about discrimination or classification. Finally, a problem that is studied in this thesis, is when an unknown object, with structures under the resolution limit, is reconstructed with enhanced resolution.

The reconstruction usually supposes that the optical system is known. Standard methods involve a direct inversion through Fourier deconvolution. Considering an isoplanatic optical system, the intensity of an image is given as convolution of the response function of the optical system with the object's intensity,

$$I_{\text{out}}(x) = \int \mathrm{d}q\, H(x-q) I_{\text{in}}(q).\tag{1.1}$$

The Fourier deconvolution is then obtained by applying Fourier transform to the previous equation and expressing it for the object

$$\mathcal{I}_{\text{in}} = \frac{\mathcal{I}_{\text{out}} + \mathcal{N}}{\mathcal{H}},\tag{1.2}$$

where $\mathcal{I}_{\text{in}}$, $\mathcal{I}_{\text{out}}$, and $\mathcal{H}$ are Fourier spectra of I_{in}, I_{out}, and H, respectively. The term $\mathcal{N}$ was added representing the spectrum of the additive noise. The spectrum $\mathcal{H}$, also called the optical transfer function, can contain singularities and vanishes beyond a certain frequency, causing a divergence [1]. Various regularization procedures were developed to mitigate this issue [2].

More sophisticated super-resolution reconstruction methods employ the rapidly growing machine-learning [3, 4], fluorescent microscopy [5, 6], or tomography

[7, 8]. Particularly, maximum-likelihood estimation and the corresponding iterative algorithm termed expectation-maximization method (also known as the Richardson-Lucy algorithm) proved to be extremely useful for image reconstruction and super-resolution [8, 9, 10, 11]. If one is interested in intensity retrieval only the Richardson-Lucy algorithm can be employed [11]. But more generally, the whole spatial information about the object in terms of its two-point correlation function, mutual intensity, can be retrieved [8]. So not only intensity but also coherence and phase properties are retrieved together with improved resolution. To do that, we have to exploit multiple scans of intensity for different settings of the known optical system. For example, the different settings of a basic imaging system, imaging through a thin lens, can be realized by changing the distance of the object to the lens, the distance from the lens to the camera, and for (even slightly) anisoplanatic systems, the transverse shift of the object from the optical axis. Generally, the more scans of intensity are provided, the better the reconstruction and thus resolution.

The structure of the thesis is as follows. A description of the reconstruction based on maximum likelihood estimation is provided in Chapter 2. A basic optical system, imaging through a thin lens, is studied. Its theoretical model is presented in Chapter 3 together with numerical simulations. Discussion of the results is presented. It is followed by experimental realization. Its description, results and their discussion is provided in Chapter 4. Conclusion is given in Chapter 5.

Chapter 2

Reconstruction of mutual intensity from multiple intensity scans

In this chapter, we will briefly outline the object imaging and its reconstruction. Let us assume an imaging system described by an amplitude point spread function $h(x, q)$. Light from an object propagates through this system and is observed–we obtain an image. Relation between the object and its image is given (in one dimension) as

$$\Gamma_{\text{image}}(x, x') = \iint \mathrm{d}q \, \mathrm{d}q' \, h(x, q) h^*(x', q') \Gamma_{\text{object}}(q, q'), \qquad (2.1)$$

where Γ_{object} and Γ_{image} are mutual intensities of an object and an image, respectively. The mutual intensity contains whole spatial information about an object. Its diagonal terms describe the object intensity, $\Gamma(q, q) = I(q)$. Off-diagonal elements determine the coherence properties and phase of the object. Coherence is the degree to which any two points (q, q') in the object can interfere, phase then tells us if the interference is constructive, destructive, or something in between. There are two limits with respect to coherence properties, the fully coherent case and the fully incoherent case. Only the complex amplitude or intensity, respectively, is of concern, in these cases.

Real imaging systems have a finite aperture, thus they are subjected to diffraction. A point is imaged as a spot, which limits the resolution. The reconstruction algorithm based on maximum likelihood estimation tries to retrieve the object mutual intensity, i.e. the information about its intensity, phase, and coherence. On top of that, it can enhance the resolution. It can be achieved by synthesis of the information from multiple intensity scans for different settings of the optical system.

When photons from the object impinge pixels of a camera, their probability distribution is multinomial and the object likelihood is given as

$$\mathcal{L}(\hat{\rho}) \approx \prod_r p_r^{n_r}, \qquad (2.2)$$

where $r = (i, j, k)$ is a multi-index, p_r is the probability that a photon will be

registered by i-th pixel on camera in the particular setting of the optical system with two degrees of freedom indexed (j, k), n_r is the number of photons that were registered by i-th pixel for the same setting, and $\hat{\rho}$ is the object represented here by its density matrix in quantum formalism. The analogy between quantum mechanics and scalar-wave theory is exploited here, which was introduced in [8].

The likelihood functional (2.2) tells us how compatible is some specified object $\hat{\rho}$ with the measured data n_r. Maximum likelihood estimation finds the object for which the likelihood reaches its maximum. Such an object must obey an extremal equation

$$\hat{R}\hat{\rho}\hat{R} = \hat{\rho}. \tag{2.3}$$

The operator $\hat{R}$ reads

$$\hat{R} = \sum_r \frac{f_r}{p_r}\hat{\Pi}_r, \tag{2.4}$$

where f_r are the relative frequencies ($f_r = n_r/N$), and $\hat{\Pi}_r$ are POVM elements (positive operator-valued measure) representing the different settings of the optical system. Detailed derivation can be found for instance in [12]. The most likely object can be found via iterating Eq. (2.3)

$$\hat{R}^{(n)}\hat{\rho}^{(n)}\hat{R}^{(n)} = \hat{\rho}^{(n+1)}. \tag{2.5}$$

Its scalar-wave counterpart can be written using x-representation of Eq. (2.5) as

$$\iint \mathrm{d}x\, \mathrm{d}x'\, \mathcal{R}^{(n)}(q, x)\Gamma^{(n)}(x, x')\mathcal{R}^{(n)}(x', q') = \Gamma^{(n+1)}(q, q'), \tag{2.6}$$

where the kernel $\mathcal{R}^{(n)}$ is the x-representation of the operator $\hat{R}$ in Eq. (2.4)

$$\mathcal{R}^{(n)}(q, x) = \sum_r \frac{f_r}{p_r^{(n)}}\mathcal{P}_r(q, x). \tag{2.7}$$

The starting point for the iterative process is the maximally mixed state or, equivalently, totally incoherent flat intensity profile. Since both the likelihood functional and the set of physically permissible mutual intensities are convex, the convergence to the global maximum is ensured.

The functions $\mathcal{P}_{ijk}$, where the multi-index is explicitly stated, given by

$$\mathcal{P}_{ijk}(q, x) = \int_{\Delta_i} \mathrm{d}x'\, h_{jk}^*(x', q)h_{jk}(x', x) \tag{2.8}$$

represent the different settings of an optical system in i-th pixel with area Δ_i. Probabilities

$$p_{ijk}^{(n)} = \int_{\Delta_i} \mathrm{d}x' \iint \mathrm{d}y\, \mathrm{d}z\, h_{jk}(x', y)\Gamma^{(n)}(y, z)h_{jk}^*(x', z) \tag{2.9}$$

are re-evaluated in each iteration for current $\Gamma^{(n)}$. The process finishes when a stop criterion is reached. Various metrics can be implemented to evaluate the quality of the reconstruction. This is discussed later in Chapter 3.

Chapter 3

Numerical simulations

3.1 Theoretical model of imaging system

We consider a basic one-dimensional optical system, imaging through a thin lens with focal length f and aperture diameter $2a$. The distance between the camera and the lens is d_{out} and is kept constant. The distance between the object and the lens is d_{in} and it is one of two parameters of the model. The second parameter is a transverse shift s of the object from the optical axis. The scheme of this optical system is depicted in Figure 3.1.
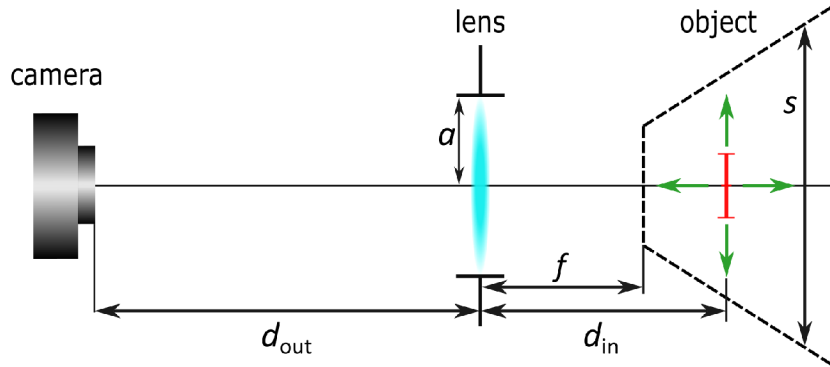

Figure 3.1: Scheme of the optical system (not to scale) with the main parameters labeled. Light propagates from right to left, from the object via the lens to the camera. The dashed lines represent the boundary values of the ranges of the two parameters–longitudinal d_{in} and transversal s shift.

The point-spread function $h(x, q) = h(x, q; d_{\text{in}}, s)$ of this optical system consists of two free evolutions and a lens transformation and can be written as

$$h(x, q) = C\, h_\infty(x, q)\mathcal{E}(x, q), \tag{3.1}$$

where

$$h_\infty(x, q) = \exp\left\{ \mathrm{i}\frac{k}{2}\left[\left(\frac{x^2}{d_{\text{out}}} + \frac{(q+s)^2}{d_{\text{in}}} - \frac{\theta^2}{\Delta} \right) \right] \right\} \tag{3.2}$$

represents the response function of the ideal system with an infinite aperture and

$$\mathcal{E}(x,q) = \frac{1}{2}\mathrm{erf}\left[\frac{1-\mathrm{i}}{2}\sqrt{k\Delta}\left(\frac{\theta}{\Delta}+a\right)\right] - \frac{1}{2}\mathrm{erf}\left[\frac{1-\mathrm{i}}{2}\sqrt{k\Delta}\left(\frac{\theta}{\Delta}-a\right)\right] \quad (3.3)$$

is the correction to the finite aperture, which approaches unity for a large aperture. The factor C in Eq. (3.1) is given as

$$C = \sqrt{\frac{2k\mathrm{i}}{\Delta d_{\mathrm{in}} d_{\mathrm{out}}}}, \quad (3.4)$$

where $k = 2\pi/\lambda$ is the wave number and the parameter Δ characterizes the defocusing from the imaging configuration,

$$\Delta = \frac{1}{d_{\mathrm{in}}} + \frac{1}{d_{\mathrm{out}}} - \frac{1}{f}. \quad (3.5)$$

The parameter θ in equation (3.2) is given as

$$\theta = \theta_{\mathrm{in}} + \theta_{\mathrm{out}} = \frac{q+s}{d_{\mathrm{in}}} + \frac{x}{d_{\mathrm{out}}} \quad (3.6)$$

and corresponds to the transverse wave number. Finally, the erf() is the error function defined as

$$\mathrm{erf}(z) = \frac{2}{\sqrt{\pi}} \int_0^z \mathrm{d}t \exp(-t^2). \quad (3.7)$$

In the special case, where $\Delta = 0$ (imaging configuration), the point-spread function is given by

$$h(x,q;\Delta=0) = C_{\Delta=0}\, h_{\infty}(x,q;\Delta=0)\mathcal{E}(x,q;\Delta=0), \quad (3.8)$$

where

$$h_{\infty}(x,q;\Delta=0) = \exp\left\{\mathrm{i}\frac{k}{2}\left[\left(\frac{x^2}{d_{\mathrm{out}}} + \frac{(q+s)^2}{d_{\mathrm{in}}}\right)\right]\right\}, \quad (3.9)$$

$$\mathcal{E}(x,q;\Delta=0) = \mathrm{sinc}(ka\theta), \quad (3.10)$$

and the factor

$$C_{\Delta=0} = \frac{ka}{\pi\sqrt{d_{\mathrm{in}} d_{\mathrm{out}}}}. \quad (3.11)$$

In our simulations, we expand on the work [8]. The particular values of the parameters of the whole system are adapted with only a few exceptions. Also, an analysis of multiple objects is presented.

The specific parameters are $\lambda = 600\,\mathrm{nm}$, $d_{\mathrm{out}} = 1.5\,\mathrm{m}$, $f = 0.5\,\mathrm{m}$, and $a = 0.6\,\mathrm{mm}$. The object is imaged when $d_{\mathrm{in}} = 0.75\,\mathrm{m}$ ($\Delta = 0$). The object is located around the optical axis, spanning up to 2 diffraction limits on each side. The diffraction limit is given as

$$R = B\lambda\frac{d_{\mathrm{out}}}{a}, \quad (3.12)$$

where B depends on the shape of the aperture as well as the coherence properties of the light. For circular aperture and totally incoherent light, it equals 0.61. For

coherent light and the same aperture 0.82. Here we are dealing with the general case of partially coherent light so we set $B = 0.5$ which is safely under (or equal to) any classical resolution limit. For the chosen parameters the diffraction limit is $R = 0.75$ mm, thus the object plane q is in the interval [-1.5, 1.5] mm and is discretized by 100 equidistant points. The corresponding mutual intensity $\Gamma(q, q')$ is given on a square mesh 100 x 100 points (q_m, q_n) in the process of data generation and subsequent reconstruction. Similarly, the output plane x is sampled by 100 pixels in the interval [-4,4] mm.

The object under examination consists of 4 sharp-edged bright spots separated by dark spaces. The spots are fully coherent with the same phase. The intensity profile of the object is depicted in Figure 3.2. All spots are 0.25 mm wide, the two middle spots are separated by 0.15 mm, the left-most and middle-left spots are separated by 0.25 mm, and the right-most and middle-right spots are separated by 0.325 mm. These separations are 5, 3, and 2 times under the resolution limit, respectively.

The reconstruction will be carried out for multiple configurations of the imaging system. We will use the notation $[j, k]$ to describe these configurations, where j represents the number of transverse positions and k the number of longitudinal positions of the object, for which data (i.e. images on camera) are gathered. That means each configuration $[j, k]$ has $j \times k$ intensity scans. We choose 26 configurations starting with [1,1] and ending with [9,6]. Some configurations have the same amount of positions distributed differently in the two parameters j and k. For example, 25 positions are distributed in configurations [1,25], [5,5], and [25,1]. The range of the parameter d_{in} is in the interval $[0.5, 0.75]$ m. The range of parameter s decreases linearly as the object is closer to the lens to compensate for the increasing magnitude and scattering of the intensity when the optical system is brought out of focus. This ensures that a substantial portion of the image is on the camera chip. For $d_{\text{in}} = 0.75$ m the range of the transverse shift is $[-1.2, 1.2]$ mm, we denote this s_0. For $d_{\text{in}} = 0.5$ m the range is $[-0.4, 0.4]$ mm, denoted s_1. The configurations that have $k = 1$ are positioned in $d_{\text{in}} = 0.75$ m (the blurred image is formed in the output plane). For configurations with j or $k > 1$, the parameters are chosen such that the boundary values of the ranges are always present. An example of a particular configuration [3,5] is given in Figure 3.2.

The data f_{ijk} were generated as follows. Firstly, the probabilities p_{ijk} in the discretized output plane were calculated via the propagation Eq. (2.1) for each j and k in given configuration $[j, k]$. Then 10^8 samples were drawn from the multinomial distribution given by probabilities p_{ijk} for the whole dataset evenly, meaning that each specific setting j and k in configuration $[j, k]$ is sampled by $10^8/jk$ samples. This yields the simulated relative frequencies f_{ijk}.

The reconstruction is an iterative process given by Eq. (2.6). We start from the totally incoherent flat intensity profile $\Gamma^{(0)}$. As a stop criterion for this process, the difference

$$\epsilon = \frac{\sqrt{\sum_{mn} |\Gamma^{(n+1)}(q_m, q_n) - \Gamma^{(n)}(q_m, q_n)|^2}}{M}, \qquad (3.13)$$

was chosen, where M is the number of elements of Γ (in our case $M = 10^4$). We consider the process finished when $\epsilon = 10^{-10}$.
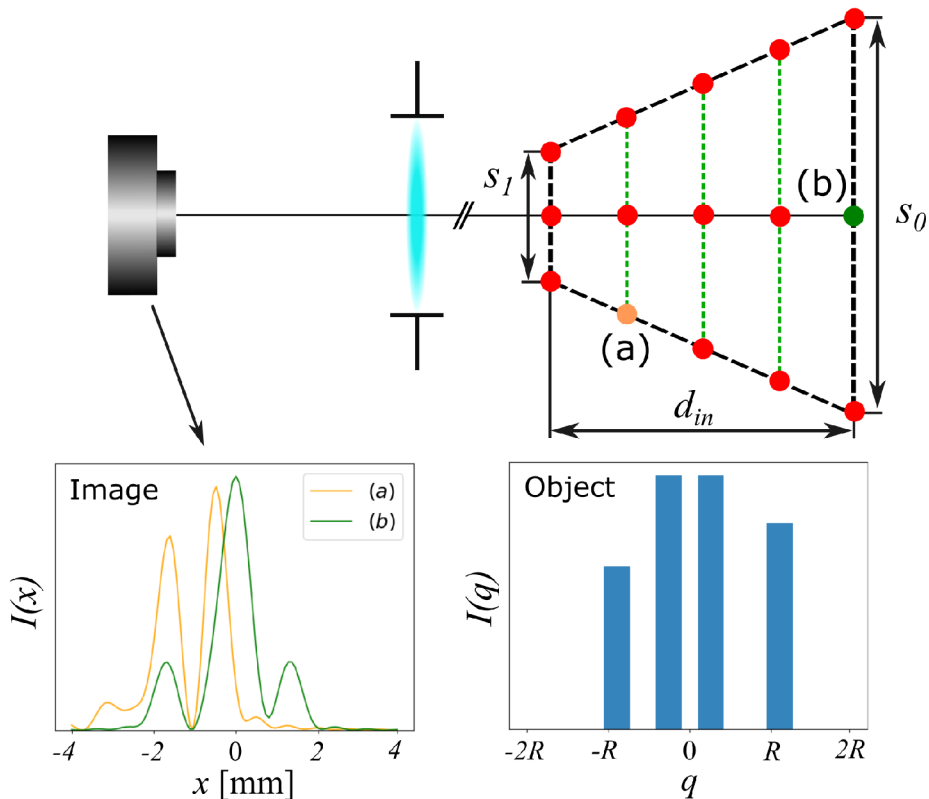
Figure 3.2: Example of one particular configuration [3,5]. Red circles represent all the positions of the object for which an image is taken. Two specific positions (a) and (b) are highlighted, and their images are provided.

We use fidelity as a measure of the quality of reconstruction. Fidelity between two mutual intensities is defined as

$$F(\Gamma, \Sigma) = \left(\mathrm{Tr} \sqrt{ \sqrt{\Gamma} \Sigma \sqrt{\Gamma} } \right)^2, \tag{3.14}$$

where Tr denotes the trace operation (sum of diagonal elements). We chose fidelity for the ease of its interpretation. It is bounded between 0 and 1, 0 meaning the two mutual intensities are nothing alike and 1 meaning they are identical. We are also going to evaluate fidelity for intensities only (diagonal of the mutual intensity matrix) given as

$$F(p, q) = \left(\sum_i \sqrt{p_i q_i} \right)^2, \tag{3.15}$$

where p and q are intensities normalized such that they represent probabilities ($\sum_i p_i = \sum_i q_i = 1$).

3.2 Results and discussion

The reconstruction algorithm was implemented in Python and fully vectorized using the NumPy and SciPy libraries. It was executed on a personal PC with quad-core processor Intel Core i5-3350P. Reconstruction for a single configuration took 2-49 seconds depending on the number of scans taken and the distribution in the two parameters j and k. Total time of 26 reconstructions took approx. 8 minutes. There is some room for speeding up the process as the code is not fully optimized.
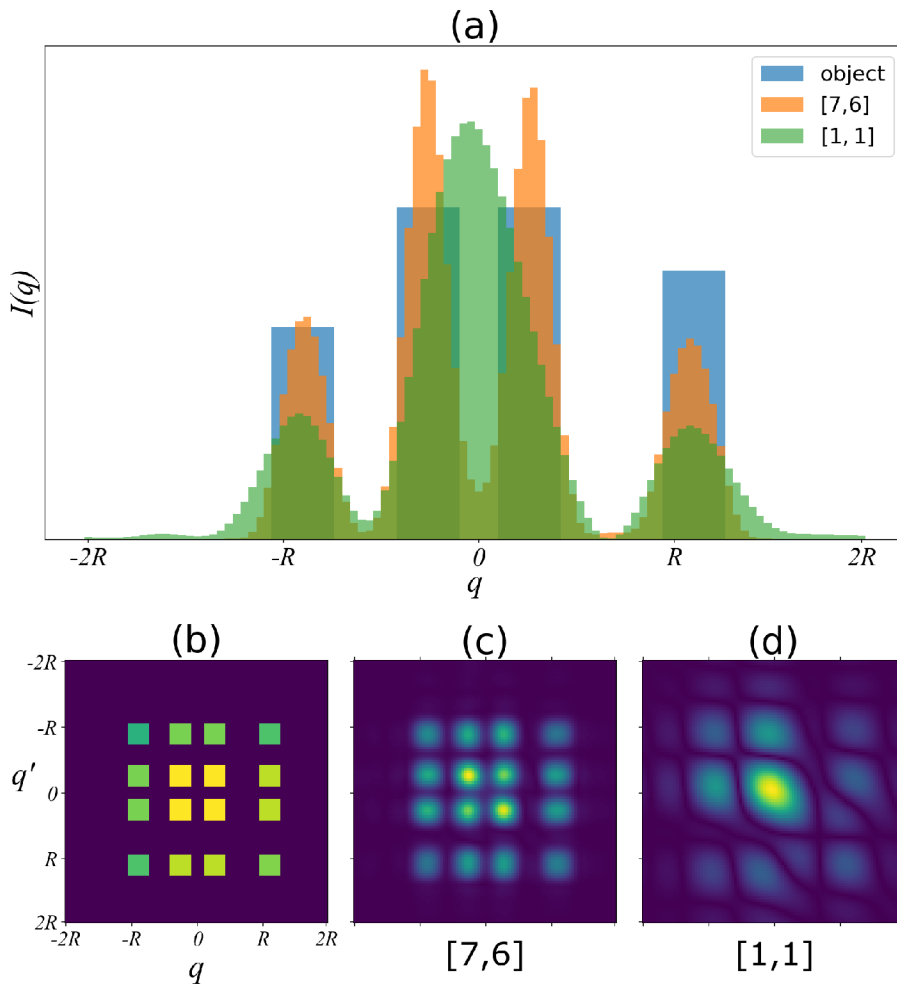
Figure 3.3: Results of reconstructions. (a) Reconstructed intensities for the best (orange) and the worst (green) performing configurations. The true object is also depicted (blue). (b) Absolute value of mutual intensity of the true object. (c) Absolute value of the reconstructed mutual intensity of the configuration [7,6]. (d) Absolute value of the reconstructed mutual intensity of the configuration [1,1].

The results for the examined object are shown in Figure 3.3. The config-

uration with the highest intensity fidelity, $F_{\mathrm{I}[7,6]} = 0.914$, was [7,6], and with the lowest [1,1], $F_{\mathrm{I}[1,1]} = 0.772$. The fact that the configuration [1,1] yields the worst reconstruction was an expected result since it had only one intensity scan to work with. Moreover, the intensity profile of this scan is the same as the reconstructed intensity (corrected for the lens transformation - scaled down and mirrored) as can be seen by comparing the Figures 3.3 and 3.2 case (b). A far more interesting result is the reconstruction for configuration [7,6]. We recall that the smallest separation (between the two middle spots) in the object is five times under the resolution limit and yet the reconstruction faithfully retrieved this structure. If we look at the reconstructed mutual intensities (their absolute values), we see that the configuration [7,6] does reveal the object MI ($F_{\mathrm{MI}[7,6]} = 0.695$), whereas the configuration [1,1] looks far more different ($F_{\mathrm{MI}[1,1]} = 0.306$).

The intensity and MI fidelities of the reconstructions for all configurations are plotted in Figure 3.4. The number of intensity scans increases or stays
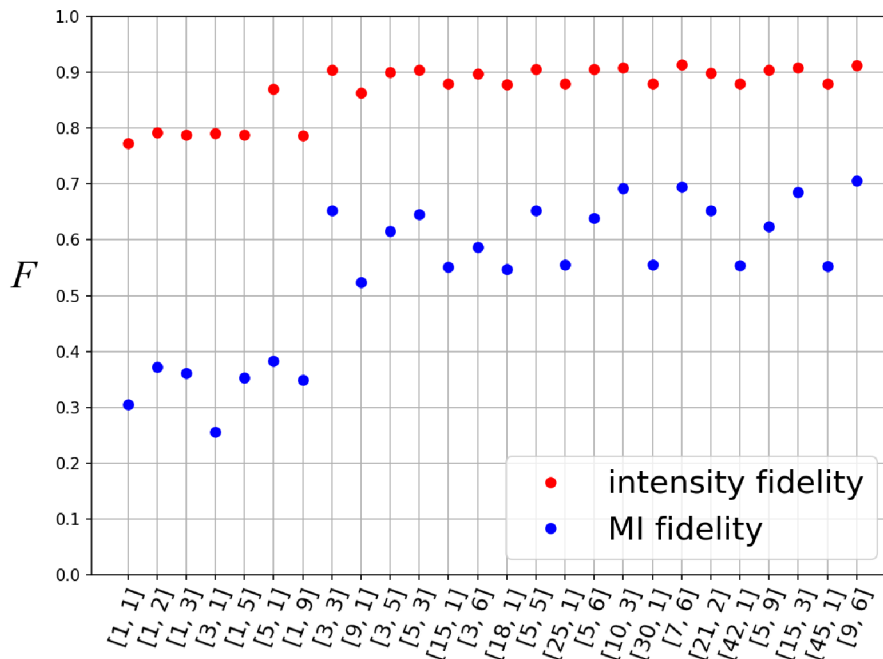

Figure 3.4: Intensity fidelity (red) and MI fidelity (blue) of reconstructions for all configurations.

the same from left to right. For configurations that have three or fewer scans, the intensity fidelity stays almost constant, then suddenly increases and after configuration [3,3] essentially saturates with slight variations depending mostly on how the positions of the object are distributed in each configuration. In the case of MI fidelity, there is no substantial increase until the configuration [3,3], where it increases rapidly. The dependence on the distribution of the positions of the object in each configuration is more evident. The top three configurations are [5,6], [7,6], and [9,6] and the MI fidelity slightly rises in that order. If we

examine this a little further, we can see some patterns. Configurations that contain only transverse positions saturate both fidelities. After configuration [15,1], for every other [j,1] (i.e. [18,1], [25,1], etc.) no increase in fidelity is observed. This hints at the fact that in the given range of the transverse shift, there is simply no more information to be obtained about the object. We tried to look for the same phenomenon for configurations that only contain longitudinal positions. And indeed they do saturate, for configurations [1,9] and onward the intensity fidelity stays at 0.787 and the MI fidelity at 0.350. These configurations are not present in Figure 3.4 as it would make it harder to read. There is one oddball configuration - [3,1]. Its MI fidelity is lower than that of configuration [1,1]. This behavior vanishes when an average performance over more objects is analyzed.

Let us now shift the attention to the fidelities of reconstructions when we average over a set of 100 random objects. Although random, these objects were generated using a few rules, to be somewhat similar in nature to the object used before. Firstly, the number of bright spots was determined by choosing a random number between 4 and 8. For each of these bright spots, the width, height, and position on the object plane is determined randomly. The bright spots are 6-11 pixels wide, which corresponds to 0.18-0.33 mm. The height has 4 levels 0.25, 0.5, 0.75, and 1. The object plane is divided by the number of bright spots, generating equidistant intervals. Each bright spot is then placed randomly in its interval. This allows for the spots to overlap. If that happens, their height is summed (only in the overlap), and it is brought back to 1 if it were to exceed it. Four examples of these randomly generated objects are given in Figure 3.5. This is by no means a perfect set of objects because what constitutes even a good set of objects is an open question.
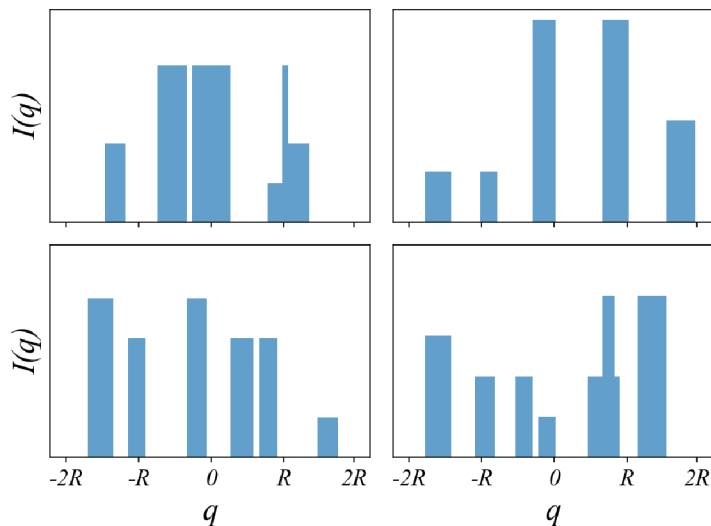

Figure 3.5: Examples of randomly generated objects by the method described in the text.

Reconstructions for this set of objects were performed for the same set of configurations. Fidelities were calculated for each configuration and averaged

over the object set. Figure 3.6 shows the average fidelities together with their standard deviations. By comparing this figure to the 3.4, we can see that the general tendencies are preserved. Although there is one substantial difference. Past the configuration [3,3], it does not matter how the positions of the object are distributed in each configuration as the fidelity saturates within the standard deviations. We might have one possible explanation for this phenomenon. The range of the transverse parameter was chosen such that the intensity of the image does not exceed the camera chip, but that holds true only for the examined object given in Figure 3.2, which is mostly confined by one resolution limit distance from the optical axis. The randomly generated objects were allowed to spread to the edges of the object plane. This caused some leakage of the image's intensity from the camera chip for positions of the object on the edges of the transverse range. We think this might have helped to even out the fidelity.

We also examined the set of configurations that contain only longitudinal positions (i.e. [1,15], [1,18], etc.), that are not present in the graph. There was no increase in any of the two fidelities beyond the [1,9] configuration.
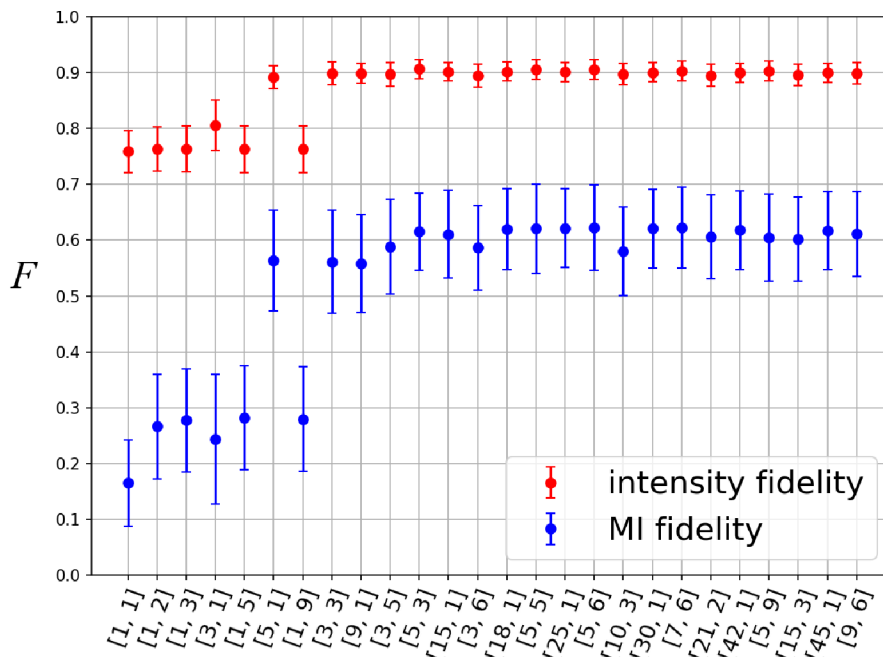

Figure 3.6: Average intensity (red) and MI fidelity (blue) of reconstructions for hundred objects and each configuration.

In conclusion, we have demonstrated that having only a few scans of intensity of a given object in different settings of the optical system can improve the reconstruction drastically, achieving super-resolution. Also, there is no point in increasing the number of scans beyond some value as the fidelity saturates, and the experimental demands rise.

Chapter 4

Experiment

4.1 Experimental setup description

A scheme of the experimental setup is shown in Figure 4.1. The setup can be divided into two parts, namely, the object preparation and the tested optical system. The former starts with a microscope objective MO_1 collimating light from a laser. The illuminated iris I_1 is imaged by a telecentric optical system consisting of lenses L_1 and L_2 onto a spatial light modulator, specifically a Digital Micromirror Device (DMD). The illuminated pattern displayed on the DMD is re-imaged by further telescope consisting of lens L_3 and microscope objective MO_2 into the object plane, hence the object plane now coincides with the working distance of the microscope objective MO_2. The second part of the experimental setup, the tested optical system, starts with the light from the object plane propagating through a lens L_t apertured by the iris I_t. The light then impinges the chip of the used camera.

Components that are not specified in the scheme description are: laser - Integrated Optics (0532L-45B) with polarization maintaining fiber and wavelength $\lambda = 532\,\text{nm}$, DMD - DLP LightCrafter 6500, camera - CCD ZWO ASI178MM with 3096 x 2080 pixels and $2.4\,\mu\text{m}$ pixel pitch. Both irises are matted. All lenses are achromatic doublets (Thorlabs).

The first telescope that creates an image of the Iris I_1 onto the DMD serves two functions. The first is to have control over the illuminated area on the DMD. The second is to make the laser beam more homogenous by magnifying (stretching) it.

The DMD consists of a 2D array of micromirrors. Each micromirror is addressed individually, causing a slight tilt ($12°$) on either side of its diagonal. The tilt on one side reflects the light toward the tested optical system, while the other tilt reflects the light away. This is a binary intensity modulation–only ON and OFF states of pixels are allowed. Nevertheless, there exist several methods enabling a full spatial phase and amplitude control of a light beam [13]. The specific DMD used (DLP LightCrafter 6500) has 1920x1080 micromirrors (14.5 x 8.2 mm). The micromirror (pixel) pitch is $7.56\,\mu\text{m}$.

Since the DMD forms a 2D grating, a vast number of diffraction orders arise. The implemented telescope consisting of L_3 and MO_2 ensures that only the zero-order passes through. Consequently, the 4.44 times demagnified object appears
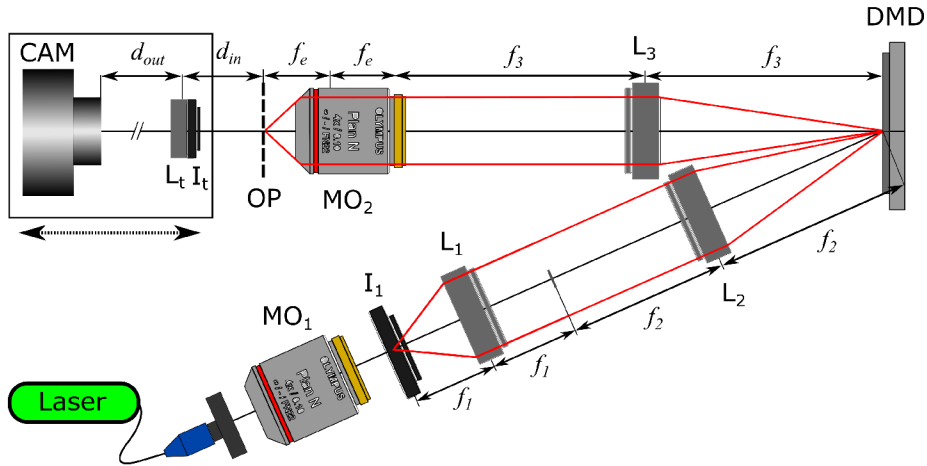
Figure 4.1: Scheme of the experimental setup. L_1, L_2, L_3 - lenses with focal lenghts $f_1 = 50\,\text{mm}$, $f_2 = 150\,\text{mm}$, $f_3 = 200\,\text{mm}$; MO_1, MO_2 - microscope objectives (Olympus) with numerical aperture NA = 0.1 and effective focal lenght $f_e = 45\,\text{mm}$; DMD - digital micromirror device; I_1 - iris that is imaged on the DMD (as the red lines indicate); OP - object plane, the DMD is re-imaged here (as the other red lines indicate); L_t - lens of the tested optical system with focal lenght $f_t = 50\,\text{mm}$; I_t - iris that is mounted on the thread of the lens L_t; CAM - camera; d_{in} distance from the object plane to the lens L_t; d_{out} distance from the same lens to the camera. The camera and the lens with the iris of the tested optical system are shown in a box indicating that they shift together.

in the focal plane of the microscope objective MO_2. The camera and the lens L_t of the tested optical system are placed onto a rail, keeping their mutual distance constant. This rail is mounted onto a linear stage with a longitudinal degree of freedom.

The object has to be able to shift transversely and longitudinally. The transverse shift is realized by simply addressing a different part of the DMD (illustrated in Fig 4.2). The longitudinal shift is realized by movement of the linear stage, on which the camera and the lens L_t are mounted (illustrated in Fig 4.1). Since the DMD micromirrors tilt around their diagonal, the whole DMD chip is mounted on a rotational stage that is 45° rotated. The camera is also rotated by 45° to unify the geometry of the DMD pixels with the camera chip.

The particular values of parameters of the tested optical system were chosen to be mostly a scaled-down versions of the values studied in previous chapter with respect to experimental feasibility. These values are $\lambda = 532\,\text{nm}$, $d_{out} = 150\,\text{mm}$, $f = 50\,\text{mm}$, $a = 1\,\text{mm}$. The resolution limit of this system is $R = 40\,\mu\text{m}$, see Eq. (3.12). The longitudinal parameter d_{in} is in the range [50, 75] mm. The transverse parameter s is in the range [-0.4, 0.4] mm for $d_{in} = 75\,\text{mm}$, again linearly decreasing to [-0.1, 0.1] mm for $d_{in} = 50\,\text{mm}$. The tested object in the object plane is produced in the range [-0.17, 0.17] mm ([-4.25R, 4.25R]), discretized by 100 points (1 point = 3.4 μm), which corresponds to 200 pixels on the DMD, where 2 pixels are considered 1 point. The output plane (a 1D
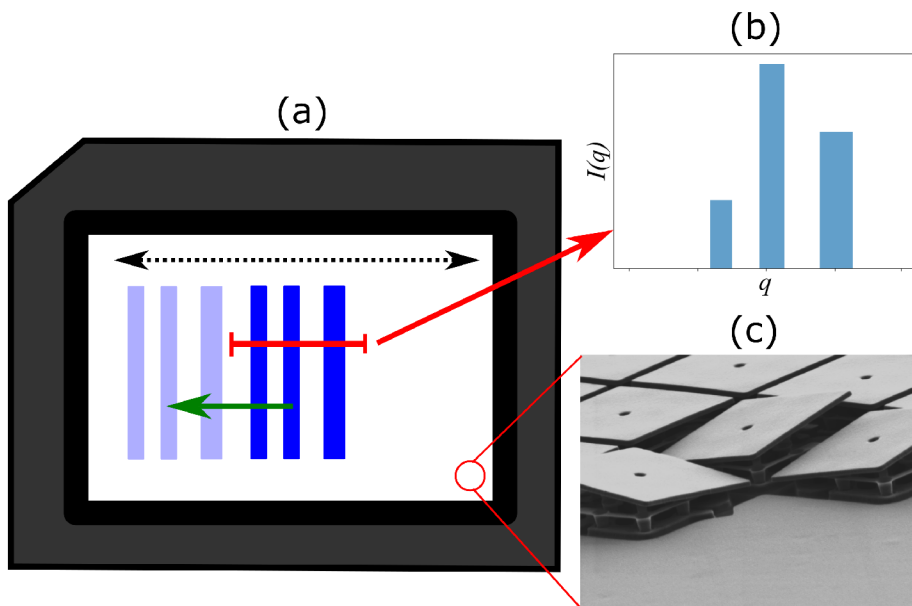
Figure 4.2: Illustration of the DMD. (a) Scheme of the DMD chip with the transverse shift of an object indicated. (b) A 1D horizontal slice of the DMD showing the object intensity profile (this profile is copied in the vertical direction). (c) A close-up photo of the DMD showing individual micromirrors (adapted from [14]).

slice of the camera chip) is discretized by 1000 points in the range [-1.2, 1.2] mm, here 1 point = 1 pixel = 2.4 μm. The object that is going to be tested is shown in Figure 4.3. The three spots on the left are each 4 points wide with 3 points separation (almost 4 times under the resolution limit). The two spots in the middle are 6 points wide with 2 points separation ($\approx R/6$). The two spots on the right are 12 and 4 points wide with 3 points separation ($\approx R/4$). We did not use the original object shown in Figure 3.2 as we wanted a more diverse structure.

In order to simulate a one-dimensional problem, the other dimension has to be unrestricted. What we mean by that is that the object modulated by the DMD in one dimension is stretched (copied) across the other. On top of that, the lens L_t in the tested optical system should be cylindrical and the diaphragm should be a slit. Unfortunately, we were restricted by available optical components. A spherical lens and an iris were used instead. This manifested itself in a distortion of the image intensity and was more prevalent for distances of the object closer to the lens. The distortion caused a nonlinear horizontal stretching of the intensity profile. Since the whole camera image is 2D, the second dimension might be exploited for a correction of this distortion.

In the following paragraphs we discuss the technical difficulties of realizing the experimental setup. Naturally, the values of the parameters are the target values. In experiment, we measured the distances mostly with a tape measure, with a millimeter precision. But the uncertainty is larger since the principal planes of lenses/microscope objectives and the position of the chip inside the
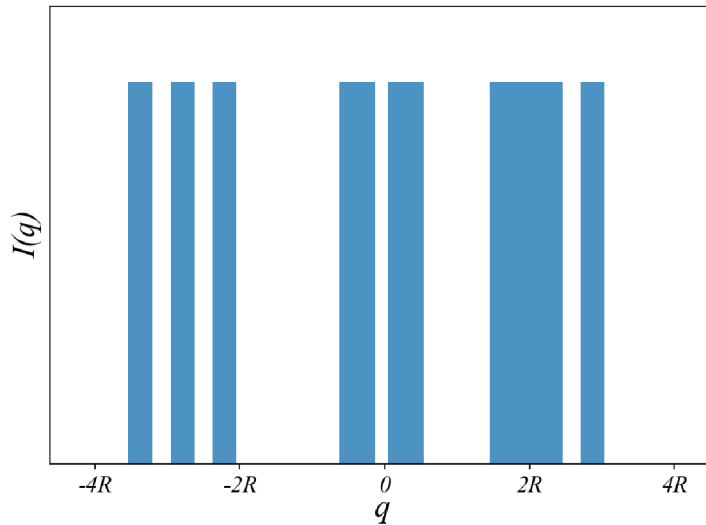
Figure 4.3: The tested object in experiment.

camera have to be guessed. To improve the guess we consulted the datasheets of the components. We think a fair uncertainty estimate is ± 3 mm.

We measured the magnification of the filtering system (L_3-MO_2) by imposing a square on the DMD and placing a camera in the working distance of the MO_2. We moved the camera until the image of the square was sharp. Then we counted the pixels of the square in both horizontal and vertical directions. We found that the magnification is (4.50 ± 0.06) in both directions. Compared to the theoretical magnification of 4.44, we deemed the system sufficiently adjusted. Similarly, we measured the magnification of the tested optical system with a theoretical magnification of 2. We found out it was (2.03 ± 0.06).

Since the iris I_t of the tested optical system was lever actuated and without a scale, we had to measure its radius. The aperture radius cannot be measured before mounting the iris on the thread of the lens L_t, because this action would induce a small but noticeable change in the radius. Thus, an auxiliary imaging system was implemented and calibrated by imaging a line USAF target placed in the iris plane. Then the iris was put back and its radius was determined from its image by fitting a circle into it. The radius of the fit in pixels was multiplied by the pixel pitch and divided by the magnification. We obtained $a = (992 + -30)$ µm. We should also point out that the iris is approximately 5 mm distant from the lens. This was as close as the mounting of the components allowed.

The motion of the linear stage, with the camera and the lens L_t mounted on, was not perfectly colinear with the direction of the propagating beam. This effectively resulted in an undesired transverse shift of the object as the distance d_{in} changed. We compensated for this by shifting the object on the DMD (and thus in the object plane). This was a crucial compensation as the maximum transverse shift induced by this imperfection corresponded to 58 µm in the object plane. A substantial value compared to the desired transverse shifts of the object.

4.2 Results and discussion

Simulation with the modified parameters and the new tested object was carried out for the same set of configurations as in Chapter 3. This time the total
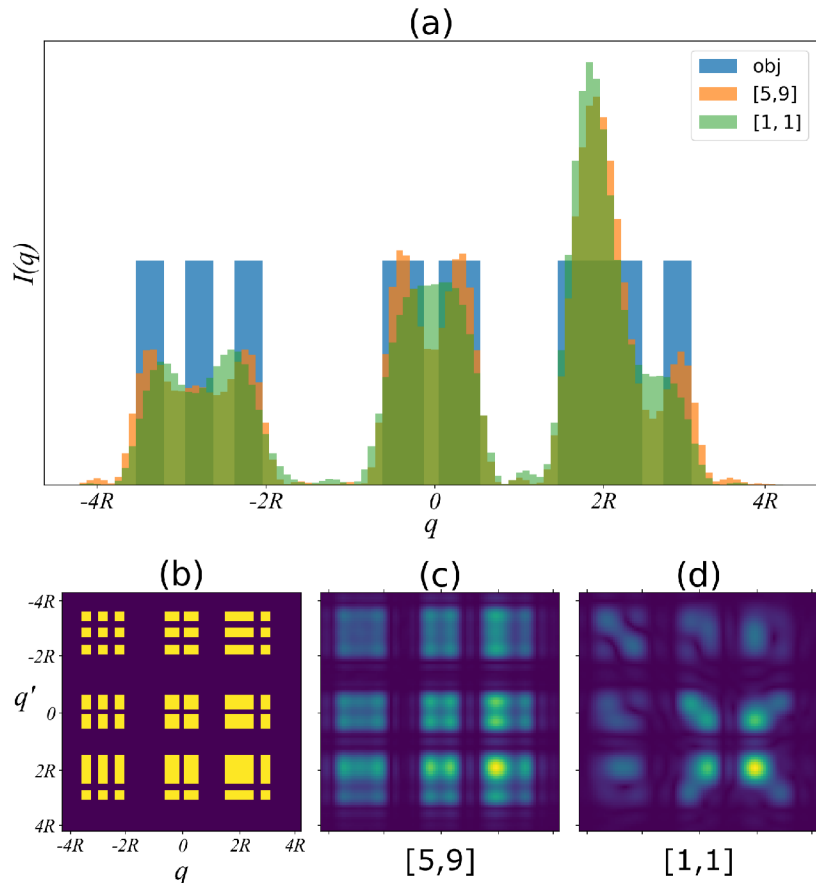

Figure 4.4: Results of reconstructions for simulation. (a) Reconstructed intensities for best and worst performing configurations. (b) Absolute value of the object's MI. (c) Absolute value of MI of the configuration [5,9] (d). Absolute value of MI of the configuration [1,1]

number of photons for the whole configuration was 3.15 million. The results for the best and the worst performing configurations (their reconstructions) are shown in Figure 4.4. The configuration [1,1] did not resolve any of the 3 main structures of the object. On the other hand, the configuration [5,9] does resolve the middle and the right structures, albeit with small contrast and over/underestimated intensities of the spots. It also struggles with the left structure of the object, with little to no improvement against the [1,1] configuration. Quantitatively, the intensity fidelity has very little disparity (0.03) between the two configurations. The fidelities are $F_{I[1,1]} = 0.846$ and $F_{I[5,9]} = 0.876$. This indicates that the intensity fidelity might not be a good metric for determining resolution enhancement. In stark contrast, the MI fidelities differ substantially,

$F_{\mathrm{MI}[1,1]} = 0.103$ and $F_{\mathrm{MI}[5,9]} = 0.753$. This is evident from Figure 4.4 cases (b), (c), and (d). The reconstructed MI (its absolute value) of configuration [5,9] does resemble the object MI very well (despite the remaining blurring). Although the configuration [1,1] has a "good idea" to put the weight in the 9 sectors dictated by the object MI, it fails inside them.

More interesting things can be inferred when we look at the fidelities of all the configurations presented in Figure 4.5. As was mentioned, the intensity fidelity
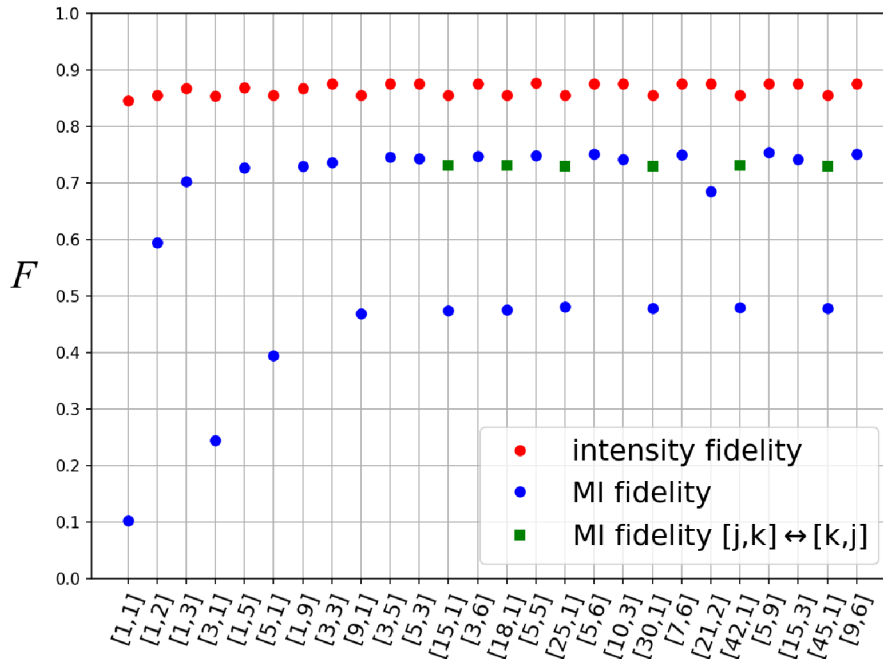

Figure 4.5: Fidelities of reconstructions for each configuration for simulation. The configurations for green points are meant to be read with swapped j and k.

differs only slightly. On the other hand, MI fidelity differs vastly and has very clear patterns. It starts low and then rises very fast. After configuration [3,5] the upper envelope becomes essentially saturated (experiencing only a tiny rise for certain configurations). Yet again, if the positions of the object in configurations are spread in one parameter only, the MI fidelity also saturates. In contrast to the simulations in Chapter 3, it is the transverse parameter where the fidelity is saturated at a lower value (0.48), whereas the longitudinal saturates at 0.73. Again, this indicates that there is no more information to be obtained, if we concern ourselves with one parameter only. Also, it is clear that the longitudinal parameter in this optical system is of more importance. Despite that, it is slightly more beneficial to include some transverse positions. This fact is further underlined if we compare the MI fidelities of the configurations [1,2] and [21,2]. The configuration [21,2] performs better, albeit with much more scans, but the number of registered counts (photons) is the same.

Why is it that in this case, the longitudinal parameter gives more informa-

tion about the object than in the previouse case, where the opposite is true? We think that the answer is hidden in the parameters of the optical setup, specifically the ratio between the aperture diameter to the object's size. In the case of the original setup in Chapter 3, the object was slightly larger than the aperture. Whereas in this case, the object is almost 6 times smaller. Also, the range of the transverse parameter is 3 times smaller in this case. The reason for this is that we were limited by the transverse shift allowed by the DMD in the experiment.
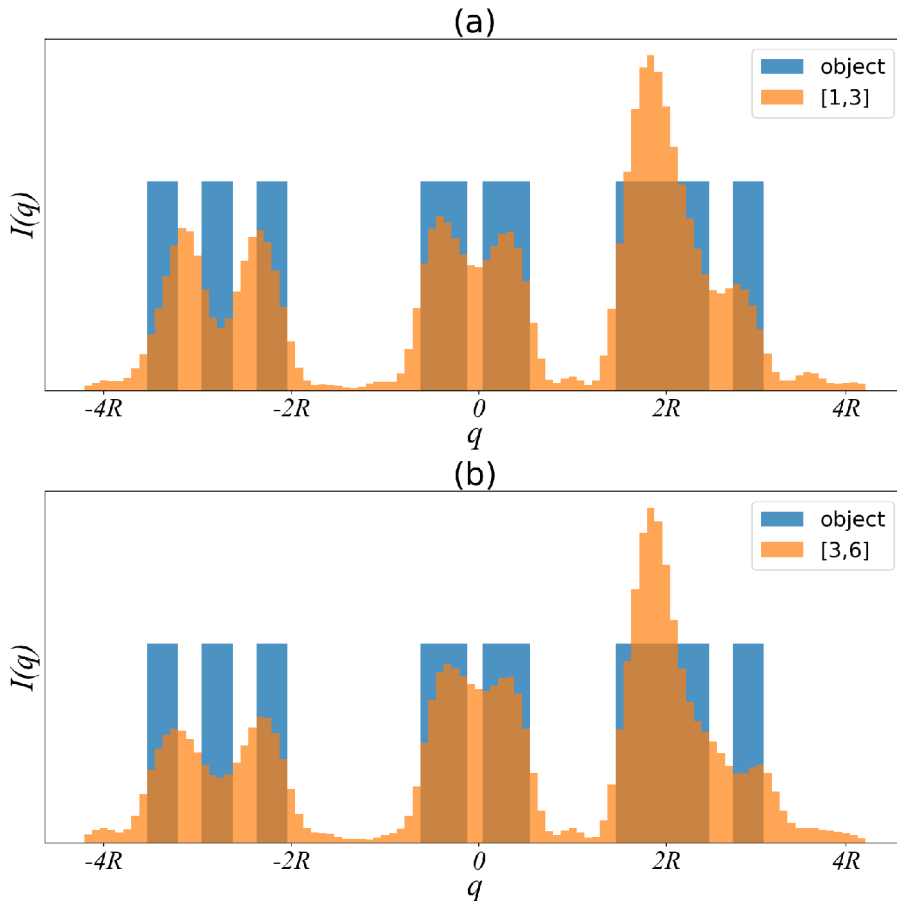

Figure 4.6: Two best reconstructed intensities from experimental data. (a) Configuration [1,3]. (b) Configuration [3,6].

Moving on to the experiment, we measured the following configurations: [1,1], [1,2], [1,3], [3,1], [3,3], and [3,6]. The exposition of the camera was set for each configuration such that there were 3.15 million counts in total (e.g. the configuration [3,6] has only 175 thousand counts per scan). This statistical sampling represents the fundamental noise termed shot noise. We were extra careful to isolate the camera chip from any stray light. Despite our best efforts to eliminate any additional noise, there was practically nothing we could do about the camera read-out and dark current noises. They created a background that was substrated in post-processing. Practically this only affected configurations

[3,3] and [3,6]. The two best reconstructions were for configurations [1,3] and [3,6]. They are shown in Figure 4.6. Interestingly enough the configuration [1,3] performed slightly better, but qualitatively those reconstructions are the same. The middle structure of the object is resolved, albeit with small contrast. It is hard to say that the structure on the right is resolved, but some similarity to the original structure is observed. The structure on the left was reconstructed as two spots instead of three. The separation of the spots in the tested object is wider than that of the middle structure, but their width is smaller, indicating that the resolution enhancement of the presented method is sensitive to the particular construction of the structures in the studied object.

The MI fidelities of reconstructions from the experiment are given in Figure 4.7. We have kept the simulation values in there for comparison and omitted the intensity fidelities. As was expected, the MI fidelities of reconstructions from
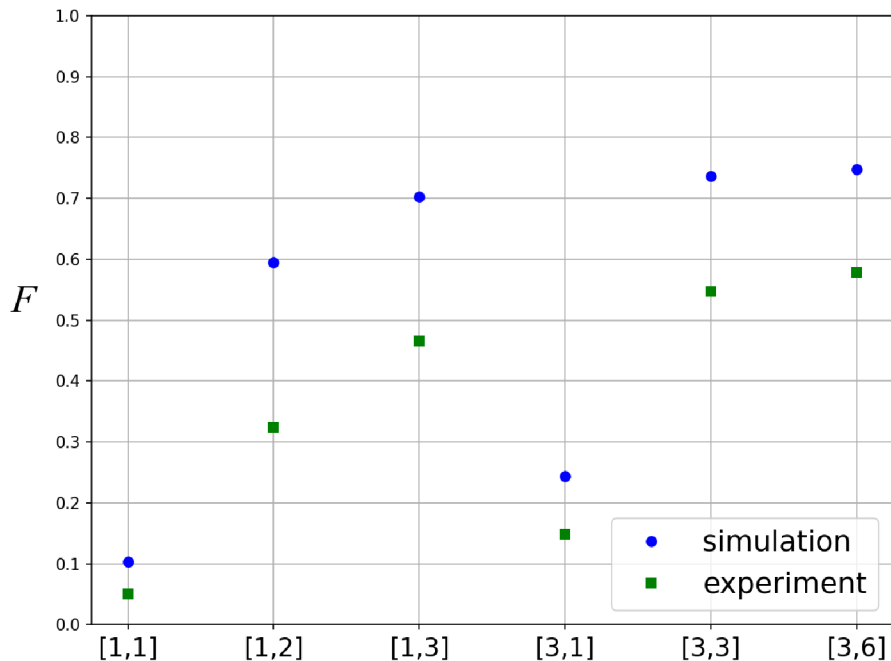

Figure 4.7: MI fidelities of reconstructions for experimentally measured configurations (green) compared to the simulations (blue).

the experimental data are lower than their simulation counterparts. The main reason behind this is the aforementioned distortion that originated from the inaccurate modeling of the 1D system in two dimensions (iris diaphragm and spherical lens were used instead of slit diaphragm and cylindrical lens). But the main tendency in the increase of fidelity as the number of positions of the object and therefore the intensity scans increases was experimentally proven. This increase in fidelity is owed more to the more faithful reconstruction of coherence properties than the resolution enhancement. This is evident from Figure 4.8, where reconstructed MIs (their absolute values) are shown for every configuration. We have also included reconstructed MIs for configurations [3,3] and [3,6]

without the post-processed data to demonstrate the effect of background noise.
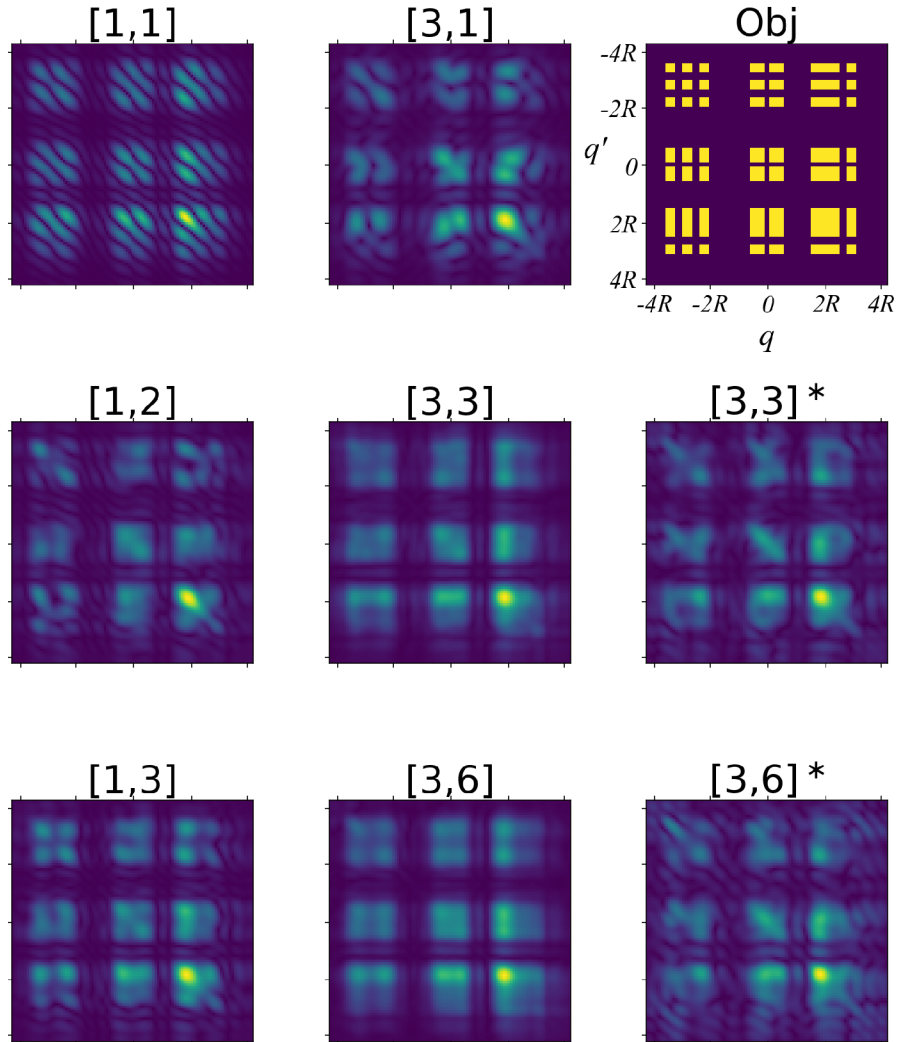

Figure 4.8: Reconstructed MIs (their absolute value) from experiment. The asterisk notes the reconstructions without the correction for background noise.

In conclusion, despite the many technical difficulties and imperfections, an increase in information gained about the object was observed, when more intensity scans were exploited. Super-resolution was achieved, albeit with small contrast and not throughout the whole object.

Chapter 5

Conclusions and outlook

The main conclusion and achievement of this thesis is that we have demonstrated experimentally feasible super-resolution imaging based on maximum-likelihood reconstruction, from several intensity scans for various settings of the imaging device. Although, it is fair to say, that this was more of a proof of concept (demonstration of the method) as the resolved distances in the object are nowhere near the state-of-the-art optical resolution. Moreover, our demonstration was performed only for 1D objects.

With our simulations, we have shown, that the increase of information gained about the object scales with the number of intensity scans taken for the different settings of the known optical system. The information gained improved the reconstruction of the object, resulting in resolution enhancement. In addition, we have shown that there is no point in increasing the number of intensity scans beyond some threshold, as the extra information about the object is exhausted, in the given range of the parameters.

In the future, we want to expand on the work done so far. For example, we want to find out where to distribute the positions of the object in the given range. We do not think that the even distribution done here is optimal. More rigorous analysis based on the Fisher information should provide the answer. We also plan to perform experiments with partially coherent light. Furthermore, we will generate arbitrary objects with DMD [13]. As the ease of execution of the experiment is concerned, the experiment could be fully automated with the addition of motorized linear stages.

In order for this work to have an impact in practice, we need to expand to two dimensions. We expect that the scalability will be a big challenge, as the reconstruction for the one-dimension already takes seconds. Further optimisation of the algorithm and its numerical implementation will be necessary.

The aim is to develop super-resolution imaging via image synthesis outperforming and complementing current methods applicable from microscopy to astronomy.

Bibliography

[1] J. W. Goodman, *Introduction to Fourier Optics*. McGraw-Hill, 1996.

[2] M. Bertero and P. Boccacci, *Introduction to Inverse Problems in Imaging*. CRC Press, 1998.

[3] C. Dong, C. C. Loy, K. He, and X. Tang, "Image super-resolution using deep convolutional networks," *IEEE Transactions on Pattern Analysis and Machine Intelligence*, vol. 38, no. 2, pp. 295–307, 2016.

[4] E. Nehme, L. E. Weiss, T. Michaeli, and Y. Shechtman, "Deep-STORM: super-resolution single-molecule microscopy by deep learning," *Optica*, vol. 5, no. 4, p. 458, 2018.

[5] S. W. Hell and J. Wichmann, "Breaking the diffraction resolution limit by stimulated emission: stimulated-emission-depletion fluorescence microscopy," *Optics Letters*, vol. 19, no. 11, p. 780, 1994.

[6] T. A. Klar and S. W. Hell, "Subdiffraction resolution in far-field fluorescence microscopy," *Optics Letters*, vol. 24, no. 14, p. 954, 1999.

[7] M. G. Raymer, M. Beck, and D. McAlister, "Complex wave-field reconstruction using phase-space tomography," *Physical Review Letters*, vol. 72, no. 8, pp. 1137–1140, 1994.

[8] M. Ježek and Z. Hradil, "Reconstruction of spatial, phase, and coherence properties of light," *Journal of the Optical Society of America A*, vol. 21, p. 1407, Aug. 2004.

[9] A. P. Dempster, N. M. Laird, and D. B. Rubin, "Maximum likelihood from incomplete data via the EM algorithm," *Journal of the Royal Statistical Society: Series B (Methodological)*, vol. 39, no. 1, pp. 1–22, 1977.

[10] Y. Vardi and D. Lee, "From image deblurring to optimal investments: Maximum likelihood solutions for positive linear inverse problems," *Journal of the Royal Statistical Society: Series B (Methodological)*, vol. 55, no. 3, pp. 569–598, 1993.

[11] W. H. Richardson, "Bayesian-based iterative method of image restoration," *Journal of the Optical Society of America*, vol. 62, no. 1, p. 55, 1972.

[12] M. Paris and J. Řeháček, eds., *Quantum State Estimation*. Springer Berlin Heidelberg, 2004.

[13] S. A. Goorden, J. Bertolotti, and A. P. Mosk, "Superpixel-based spatial amplitude and phase modulation using a digital micromirror device," *Optics Express*, vol. 22, no. 15, p. 17999, 2014.

[14] Texas Instruments. `https://e2e.ti.com/resized-image/__size/450x0/__key/communityserver-blogs-components-weblogfiles/00-00-00-09-72/DLP-MEMS-blog-1.png`, 2016. [Online; accessed April 15, 2023].